Journal of Physics and Chemistry of Solids 153 (2021) 110011

Contents lists available at ScienceDirect

Journal of Physics and Chemistry of Solids

journal homepage: http://www.elsevier.com/locate/jpcs

Stability, and electronic and optical properties of ternary nitride phases of $MgSnN_2$: A first-principles study

B.B. Dumre [a], D. Gall [b], S.V. Khare [a,*]

[a] Department of Physics and Astronomy, The University of Toledo, Toledo, OH, 43606, USA
[b] Department of Materials Science and Engineering, Rensselaer Polytechnic Institute, Troy, NY, 12180, USA

ARTICLE INFO

Keywords:
$MgSnN_2$
Disordered rocksalt structure
Electronic properties
Optical properties
Mechanical properties

ABSTRACT

We have studied the disordered rocksalt, orthorhombic, and disordered wurtzite phases of the ternary nitride semiconductor $MgSnN_2$ by first-principles methods using density functional theory (DFT) and beyond. The results imply that $MgSnN_2$ is mechanically and dynamically stable in all three phases. However, pCOHP analysis suggests that the disordered rocksalt structure has antibonding states below the Fermi level between −5 eV and −2 eV, as compared to the bonding states in the other two phases, indicative of its thermodynamic metastability. Computed lattice constant and electronic band-gap values of 4.56 Å and 2.69 eV for $MgSnN_2$ in the disordered rocksalt structure compare well with experimentally reported values of 4.48 Å and 2.3 eV, respectively. Furthermore, band gaps were computed for $MgSnN_{2-x}O_x$ ($x = 0.5, 1.0, 1.5, 2.0$) to elucidate the role of possible oxygen impurities. Band-gap bowing is suggested to occur upon alloying with oxygen. Of the three phases, the disordered rocksalt structure shows the lowest charge carrier effective masses. Moreover, the absorption coefficient and reflectivity of this phase make it promising for use as the absorber layer of tandem solar cells in the higher energy region of the visible portion of the solar spectrum. The other two phases, disordered wurtzite and orthorhombic, might be utilized as the window layer of solar cells owing to their larger band-gap values of 4.36 eV and 4.86 eV, respectively.

1. Introduction

Inorganic nitrides have been historically divided into two main groups based on their electronic properties, namely semiconductor wurtzite main group metal nitrides and superconducting rocksalt transition metal (TM) nitrides [1]. Exceptions include semiconducting rocksalt nitrides (e.g., ScN) [2] and metallic wurtzite nitrides (e.g., $ZnMoN_2$) [3]. The nitrides of the first type, that is, semiconducting wurtzites such as AlN, GaN, and InN, are well known for their direct band-gaps and high carrier mobilities [4,5]. They are widely used in solid-state lighting, radiofrequency transistors, laser diodes, high-data-density optical storage media, and so on [4–9]. The second type, superconducting rocksalt TM nitrides, such as TiN, VN, and NbN, are utilized in hard coatings [10–13], and as diffusion barriers in semiconducting devices and superconductors with transitions at temperatures of the order of 20 K [13,14].

Ternary nitride semiconductors with rocksalt structure of formula II-IV-N_2 have been widely studied in the past decade [15]. They are obtained by replacing metal atoms in a binary metal nitride with Group II^{2+} and Group IV^{4+} atoms. For example, a metal such as Ti has the 3+ valence state in its nitride (TiN) [16]. Inserting a low-valent alkaline-earth cation such as Mg^{2+} results in $MgTiN_2$, forcing the TM to adopt a higher oxidation state, prohibiting the metal d-shell from engaging in bonding, and thereby introducing semiconductor properties [17–20]. Moreover, cation- and anion-substoichiometric defect phases are found in binary TM nitrides with rocksalt structure [21–23]. This implies the possibility of newly inserted alkaline-earth cations occupying metal site vacancies [1].

Epitaxial growth of these new ternary nitrides on multiple substrates is facilitated by congruent lattice parameters. Thus, they can be meticulously grown over their binary semi- and super-conducting antecedents [1]. These nitrides are synthesized from highly Earth-abundant and non-toxic metals and are semiconducting [24]. Moreover, the relatively low cost and ease of recyclability of the constituent metals such as Zn, Mg, and Sn in comparison to In and Ga makes them promising for scalable electronic applications. Examples such as $ZnSnN_2$, $MgSnN_2$, $MgHfN_2$, Mg_2NbN_3, and $MgZrN_2$ have electronic band gaps in the range 1.5–3.5 eV, akin to those of their binary counterparts AlN, InN, and GaN,

* Corresponding author.
E-mail address: sanjay.khare@utoledo.edu (S.V. Khare).

https://doi.org/10.1016/j.jpcs.2021.110011
Received 12 August 2020; Received in revised form 19 February 2021; Accepted 20 February 2021
Available online 26 February 2021

which are optimal for visible and short-wavelength opto-electronic device applications [25,26]. These ternary nitride semiconductors also overcome the issue of lattice mismatch. AlN-based hetero-structures, such as AlGaN, InGaN, and InAlGaN, exhibit lattice mismatch and polarization, reducing the efficiency of devices, although this has been mitigated in more recently studied ternary systems [27].

Despite these possibilities, only a few such systems, such as $BaHfN_2$, $SrHfN_2$, and $SrTiN_2$, have hitherto been synthesized [28–31]. Recently, a new ternary nitride semiconductor with a disordered rocksalt structure, $MgSnN_2$, was synthesized by Kawamura et al. [24], which showed interesting material properties. These authors reported that $MgSnN_2$ was synthesized by a metathesis reaction under a high pressure of 5.5 GPa at 850 °C for 1 h. The product adopted a disordered rocksalt structure with a lattice constant of 4.48 Å and a direct electronic band gap of 2.3 eV. The possibility of 9.4% oxygen impurity in the anionic position was suggested by energy-dispersive X-ray (EDX) measurements. Besides the rocksalt structure, orthorhombic and wurtzite structures of $MgSnN_2$ [25,32,33] are also well known, as synthesized and characterized by Makin et al. They reported many intermediate structures between these two phases characterized by disorder in the cationic site, quantified by the long-range order parameter 'S' (defined as $S = r_\alpha + r_\beta - 1$, where r_α and r_β are the fractional occupancies of Mg and Sn, respectively, at their ordered positions) [25]. Greenaway et al. recently synthesized $MgSnN_2$ in a mixed rocksalt-wurtzite phase with stoichiometric values of Mg/(Mg + Sn) ranging from 0.28 to 0.73, and characterized the absorption properties of these products by means of spectroscopic ellipsometry [34]. Their computations, using the kinetically limited minimization (KLM) approach and electronic properties, predicted various crystal structures, with varying formation energies in wurtzite, zinc blende, and rocksalt crystal structures. Other preliminary work on the orthorhombic structure has involved computations of band structure and elastic constants using generalized gradient approximation (GGA) pseudopotentials [32,33]. However, a combined and holistic study of these three $MgSnN_2$ phases is essential to provide insight into the origin of experimental observations. Therefore, we present here a thorough computational investigation of the structural, energetic, bonding, thermodynamic, mechanical, vibrational, and optical properties of $MgSnN_2$.

To fully elucidate the behavior of $MgSnN_2$, we have analyzed and compared all three crystal structures. The main findings of this work are as follows. (i) All three phases of $MgSnN_2$, disordered rocksalt, orthorhombic, and disordered wurtzite, are both mechanically and dynamically stable. (ii) Calculated lattice constants and electronic band gaps are in good agreement with experimental results [24]. The calculated band gap is indirect, whereas the experimentally reported one is direct. (iii) Computations of $MgSnN_2$ alloyed with oxygen to analyze the effects of possible oxygen impurities imply bowing of the band-gap plots. (iv) The disordered rocksalt structure has lower effective masses than the other two crystal structures. Analysis of absorption coefficient and reflectivity indicates that the disordered rocksalt structure may be suitable as an absorber layer for solar cells operating in the higher energy region of the solar spectrum, as used in tandem devices. The other two crystal structures may serve as window layers of solar cells.

2. Computational methods

The Vienna ab initio simulation package (VASP) [35–38] was used for all density functional theory (DFT) calculations. The Perdew–Burke–Ernzerhof (PBE) [39,40] exchange-correlation functional was deployed in the generalized gradient approximation (GGA) to perform the projector-augmented-wave (PAW) method [41,42]. Along with the outer core, semi-core electrons were included in the calculations. PAW PBE VASP pseudopotentials, i.e. 'N_s', 'Sn_d', and 'Mg_sv', were used. Plane waves of energy cut-off up to 500 eV were used with a Γ-centered k-point mesh, leading to 4000 k-points per reciprocal atom (KPPRA) in our calculations. Each atom was configurationally relaxed until the forces were under 0.01 eV/Å, and convergence in energy in electronic iterations of 10^{-6} eV/atom was used when deploying a Gaussian smearing of width 0.2 eV. At the inception, initial crystal structures were taken from the Materials Project [43].

Formation energy is defined as the difference in energy between the final products and the reactants in a chemical reaction [44–46]. After relaxation, high-precision static calculations were conducted to calculate the accurate ground-state energies of the reactants and products to calculate formation energy. Formation energy per formula unit of $MgSnN_{2-x}O_x$ was calculated as:

$$\Delta E_f = E(MgSnN_{2-x}O_x) - E(Mg) - E(Sn) - (2-x)E(N_2)/2 - xE(O_2)/2 \quad (1)$$

where E(Mg), E(Sn), $E(N_2)$, and $E(O_2)$ are the ground-state energies of magnesium (space group: $P6_3/mmc$), tin (space group: $I4_1/amd$), and nitrogen and oxygen dimers in vacuo, respectively.

Computations involving strained supercells were performed to calculate elastic constants by calculating the Hessian matrices of directional second derivatives of energy with respect to cell distortion [45,47–54]. Thus, we obtained the elastic tensor (C_{ij}) for each structure, from which the mechanical properties were derived by the Voigt–Reuss–Hill [55–60] method, as described below:

The bulk and shear moduli in the Voigt approximation are given by:

$$B_V = [C_{11} + C_{22} + C_{33} + 2(C_{12} + C_{13} + C_{23})]/9, \text{and} \quad (2)$$

$$G_V = [(C_{11} + C_{22} + C_{33} - C_{12} - C_{13} - C_{23}) + 3(C_{44} + C_{55} + C_{66})]/15 \quad (3)$$

respectively. Similarly, in the Reuss approximation, they are given by:

$$B_R = [(S_{11} + S_{22} + S_{33}) + 2(S_{12} + S_{13} + S_{23})]^{-1}, \text{and} \quad (4)$$

$$G_R = 15[4(S_{11} + S_{22} + S_{33} - S_{12} - S_{13} - S_{23}) + 3(S_{44} + S_{55} + S_{66})], \quad (5)$$

respectively, where S_{ij} is the elastic compliance tensor obtained as the inverse of elastic tensor C_{ij}. In the Hill approximation, the average bulk and shear moduli are given by:

$$B = (B_V + B_R)/2 \text{ and } G = (G_V + G_R)/2 \quad (6)$$

respectively. Eventually, Pugh's ratio and Vickers hardness can be obtained by:

$$\kappa = G/B \text{ and } H_V = 0.92\kappa^{1.137}G^{0.708} \quad (7)$$

respectively, as elaborated by Tian et al. [61–64].

Electronic band gaps are underestimated by the GGA and local density approximation (LDA) exchange-correlation functionals [65]. Therefore, in such calculations, we applied the Heyd–Scuseria–Ernzerhof hybrid functional (HSE06) [66,67], which combines 25% of the exact exchange from Hartree–Fock theory with 75% of the exchange from GGA. This function has been shown to predict experimental results more accurately in the context of semiconductors and insulators [49,65,68,69]. We deployed a smaller k-point grid of 2000 KPPRA in these calculations to reduce the computational burden [49,70] and calculated the electronic density of states (DOS), band structure, and frequency-dependent complex dielectric function ($\varepsilon_1 + i\varepsilon_2$) for cation-disordered $MgSnN_2$. Effective masses (m*) of holes (m_h/m_o) and electrons (m_e/m_o) were obtained through band-structure calculation using the Sumo [71] package, where m_h and m_e are hole and electron masses, respectively, within the material and m_o is the standard electron rest mass.

To gain further insight into the chemical bonding, we calculated crystal orbital Hamilton populations (COHPs) using the local-orbital basis suite towards electric-structure reconstruction (LOBSTER) package [46,48,62,72–78]. Furthermore, to assess the charge transferred in the formation of the compound, we calculated effective charges by Bader analysis [79–82]. To elucidate the development of phonons and their behavior, we used the Phonopy [83] package to calculate phonon DOS and band structure for cation-disordered $MgSnN_2$.

3. Results

3.1. Structural, mechanical, and vibrational properties

Recently, experimental synthesis of $MgSnN_2$ yielded a cation-disordered rocksalt-derived structure. Experimental EDX measurements revealed a possible oxygen impurity of 9.4% in anionic positions [24]. Motivated by this finding, we started out with a conventional cell of eight atoms in rocksalt structure (space group: $Fm\bar{3}m$). Then, we substituted all 4a Wyckoff positions by two atoms each of Mg and Sn. Furthermore, all 4b Wyckoff positions were substituted by N or O atoms in different stoichiometries. The materials thus formed were $MgSnN_2$, $MgSnN_{1.5}O_{0.5}$, MgSnNO, $MgSnN_{0.5}O_{1.5}$, and $MgSnO_2$, with the disordered rocksalt structure (space group: $P4/mmm$). We proceeded to perform DFT calculations for all 96 possible permutations of the eight-atom conventional cell. These structures of $MgSnN_{2-x}O_x$ ($x = 0.0$, 0.5, 1.0, 1.5, 2.0) with the disordered rocksalt phase are described in Tables S1–S5, including sample structures used for computations. For comparison, we also investigated $MgSnN_2$ in wurtzite-derived and ordered orthorhombic crystal structures, which have been studied both theoretically [32,33,84,85] and experimentally [25]. To create a cation-disordered wurtzite-derived (space group: $P6_3mc$) crystal structure, we randomly substituted Mg and Sn atoms in a 1:1 ratio in the 2a cation Wyckoff positions, whereas we substituted N atoms in the two other 2b Wyckoff positions, as shown in Table S6. The two possible permutations of the cation-disordered wurtzite-derived crystal structure of $MgSnN_2$ (space group: $P3m1$) were constructed with a conventional cell of four atoms. All permutations, 96 in the disordered rocksalt structure and 2 in the disordered wurtzite structure, resulted in identical values for all computed properties. The results reported in this work relate to the structures presented in Table S1. To thoroughly understand the effects of disorder, larger supercells would have to be investigated, demanding prohibitive computational resources. Such a study of the details of the disorder is beyond the scope of the current work, and may require other techniques [86–88]. We obtained the ordered orthorhombic crystal structure of $MgSnN_2$ directly from the Materials Project database [43]; it has 16 atoms in the conventional cell; 8 cationic and 8 anionic sites, as shown in Table S7. Computed lattice constants for various crystal structures of $MgSnN_{2-x}O_x$ are given in Table 1. The structure of primary interest here, disordered rocksalt, has a calculated lattice constant of 4.56 Å, close to the experimental value of 4.48 Å [24]. In our study, all of the disordered rocksalt crystal structures have octahedral arrangements with coordination number six, whereas the disordered wurtzite and orthorhombic crystal structures have tetrahedral arrangements with coordination number four. The average bond lengths from Mg, Sn, and N to the first nearest neighbors within each crystal structure are given in Supplementary Table S8. The average bond length is 2.28 Å at each element in the disordered rocksalt structure as a result of its cubic symmetry. However, the average bond lengths at each element are different in the other two phases. Interestingly, values of 2.12 Å and 2.09 Å are interchanged for Mg and Sn between the orthorhombic and disordered wurtzite crystal structures. The bond lengths at N in these two phases are 2.10 Å, equal to the average of all bond lengths at each element.

The formation energies of the three different crystal structures are also given in Table 1. Evidently, the orthorhombic phase has a lower formation energy per formula unit, making it more stable than the other two forms of $MgSnN_2$. Despite being energetically metastable, the disordered rocksalt and wurtzite crystal structures appear to be mechanically and vibrationally stable, as discussed below.

Solar panels are subject to mechanical stresses due to variations in temperature, wind, snow or dust covering, mechanical loading in assembly, transport, and installation [89]. In order to consider the effects of such mechanical stresses, we computed a variety of elastic and mechanical constants and stability conditions. Several of these, namely bulk modulus, shear modulus, Pugh's ratio, and Vickers hardness, for the respective crystal systems of $MgSnN_2$, are given in Supplementary Table S9. The elastic constants are higher for the disordered rocksalt structure than for the other two phases. Moreover, $MgSnN_2$ has lower elastic constants than those evaluated in earlier computations on $MgSiN_2$ and $MgGeN_2$ in the orthorhombic crystal structure [32]. A general softening of the material with the introduction of heavier elements is observed. We assessed stability conditions [90] and found that all of the crystal structures are mechanically stable. The bulk and shear moduli in the three phases decrease in the order: disordered rocksalt > orthorhombic > disordered wurtzite. The Pugh's ratio is 0.75 for the disordered rocksalt structure and 0.49 for the other two phases. All three phases have a low value of Pugh's ratio, implying ductility. Among them, the disordered rocksalt structure is the least ductile. The Vickers hardness of the disordered rocksalt structure of $MgSnN_2$ is 17.76 GPa, higher than those of the orthorhombic (7.59 GPa) and disordered wurtzite (6.97 GPa) crystal structures. It is also higher than those of Si (11.77 GPa) [91] and CdTe (0.49 GPa) [92]. Thus, $MgSnN_2$, in all of these structures, is a mechanically robust candidate for use in solar cells.

To investigate thermal stability with regard to lattice vibrations, we calculated band structure and DOS for phonons for all three crystal systems, as plotted in Fig. 1. For each structure, there is no phonon population below zero frequency, which clarifies that all the phonons are dynamically stable in these crystal phases. Further, we can distinguish that N gives rise to prominent peaks in the higher frequency range around 10 THz, the Mg peaks are around 5–10 THz, and the Sn peaks are below 5 THz in each of the crystal structures. This reflects the fact that lighter particles have higher vibrational frequencies than heavier ones. In the orthorhombic and wurtzite structures, a gap is apparent in the phonon bands, whereas no such gap is seen for the disordered rocksalt structure. Due to these phonon band gaps, we surmise that the

Table 1
Lattice constants of $MgSnN_{2-x}O_x$ in different crystal structures, along with their formation energies per formula unit, calculated using the GGA. Experimental values are given in parentheses.

Material	Crystal Structure		Lattice Constants (Å)			Formation Energy (eV)
	Name	Space Group	a	b	c	
$MgSnN_2$	disordered rocksalt	$P4/mmm$	4.56 (4.48[p])	$= a$	$= a$	−3.18
$MgSnN_2$	disordered wurtzite	$P3m1$	3.44	$= a$	5.58	−3.64
$MgSnN_2$	orthorhombic	$Pna2_1$	5.54, 5.47[q]	5.97, 5.91[q]	6.94, 6.88[q]	−4.12, −1.32[r], −2.16[s], −3.41[t]
$MgSnN_{1.5}O_{0.5}$	disordered rocksalt	$P4/mmm$	4.63	$= a$	$= a$	−4.84
MgSnNO	disordered rocksalt	$P4/mmm$	4.71	$= a$	$= a$	−6.44
$MgSnN_{0.5}O_{1.5}$	disordered rocksalt	$P4/mmm$	4.77	$= a$	$= a$	−8.31
$MgSnO_2$	disordered rocksalt	$P4/mmm$	4.86	$= a$	$= a$	−9.94

[p] Ref. [24].
[q] Ref. [32].
[r] Ref. [84].
[s] Ref. [43].
[t] Ref. [33].

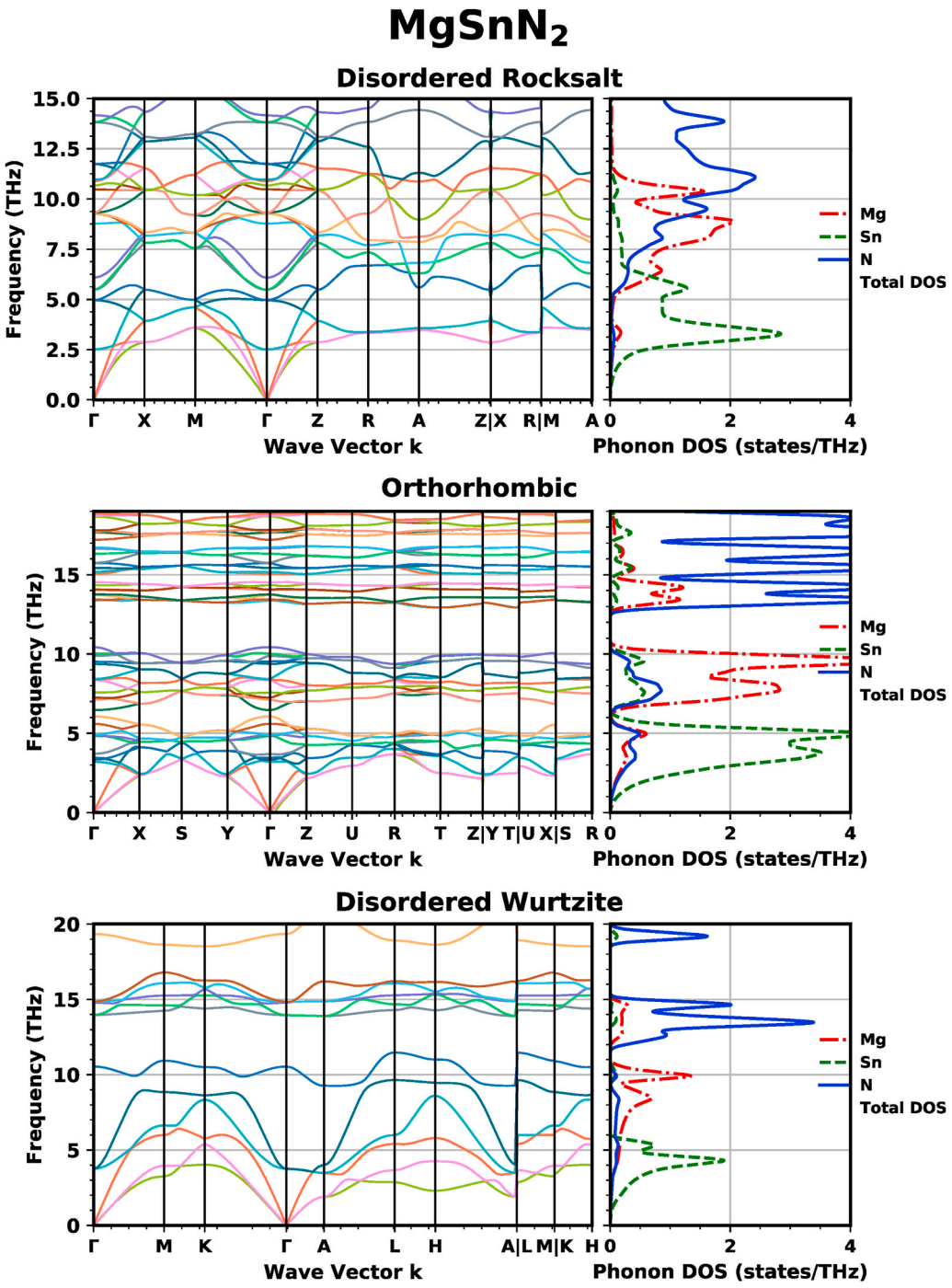

Fig. 1. Comparison of phonon band structures and densities of states (DOS) per unit cell of $MgSnN_2$ for different crystal structures, computed using the GGA.

orthorhombic and wurtzite structures might be used as sound filters and ideal mirrors, because any frequency within the gap will not propagate in the material and hence will be reflected from its surface [93].

3.2. Electronic properties

The electronic density of states (DOS) for each structure of $MgSnN_2$, computed using the HSE06 functional, is displayed in Supplementary Fig. S1. We observe that Sn and N states are more pronounced than Mg states both above and below the Fermi level in each structure. Above the Fermi level, states start to appear after the band gap in each structure, confirming the non-metallic behavior of these materials. To augment these findings, we also plotted projected crystal orbital Hamilton population (pCOHP) vs. energy, as shown in Supplementary Fig. S2, which provides insight into the bonding and antibonding characteristics of the electronic states. As electronic states are loosely bound above the Fermi level in the conduction band, the pCOHP curves above the Fermi level are in antibonding states in all three crystal structures. In the orthorhombic and wurtzite structures, the interactions of both Mg and Sn with N are seen to have bonding character. The total net interactions in these structures, shown in green dot-dashed lines, show that they are positively bonded. However, in the disordered rocksalt structure, the interactions of both Mg and Sn with N, as well as the total net interaction in the material, show an anti-bonding area between −5 eV and −2 eV, i.e., below the Fermi level. From inspection of the electronic states in Supplementary Figs. S1 and S2, one may deduce that there is an

instability in the disordered rocksalt structure. This inference is supported by the highest formation energy of the disordered rocksalt structure, as given in Table 1, and the subsequent phonon contribution to the stability as given in Fig. 1. However, the experimental synthesis of this material is testament to its thermodynamic stability. This stability may have been due to an oxygen impurity, as discussed in relation to the experimental work [24]. Alternatively, the metastability does not preclude its synthesis through kinetic pathways under the applied experimental conditions. We compared this antibonding area to the coordination number of four in the orthorhombic and disordered wurtzite crystal structures vs. six in disordered rocksalt structure. Due to the higher coordination number in the disordered rocksalt structure, the same elements, Mg, Sn, and N, behave differently.

The electronic DOS, computed using the HSE06 functional, and the pCOHP curves of all nearest-neighbor interactions for the disordered rocksalt structure of $MgSnO_2$ are displayed in Supplementary Fig. S3. Similar to the situation for $MgSnN_2$, Mg states are less pronounced than Sn and O states both above and below the Fermi level in each structure. Overall, the electronic states in $MgSnO_2$ manifest in a similar manner to those in $MgSnN_2$, as described in the preceding paragraph. Finally, the electronic DOS, computed using the HSE06 functional, for $MgSnN_{2-x}O_x$ ($x = 0.5$, 1, and 1.5) are displayed in Supplementary Fig. S4. Metallic behavior is evident for all of the compounds, with some states around the Fermi level.

In order to identify the bonding type, viz. ionic or covalent, prevalent between Mg and N or Sn and N, we deduced the effective charges on these atoms in order to elucidate the charge transferred from the electropositive to the electronegative atom. Supplementary Table S10 shows the charges transferred from Mg to N and from Sn to N in all three crystal structures considered here. There is no difference in the charge transferred value of 1.66 *e* from Mg to N in any of the crystal structures, but there is a slight variation in the charge transferred from Sn to N, increasing from 1.70 *e* in wurtzite, to 1.72 *e* in rocksalt, to 1.78 *e* in the orthorhombic form. Since the values of charge transferred from Mg and Sn to N are in excess of 1 *e*, it can be stated that these bonds have significant ionic character. The higher charge-transfer value from Sn to N

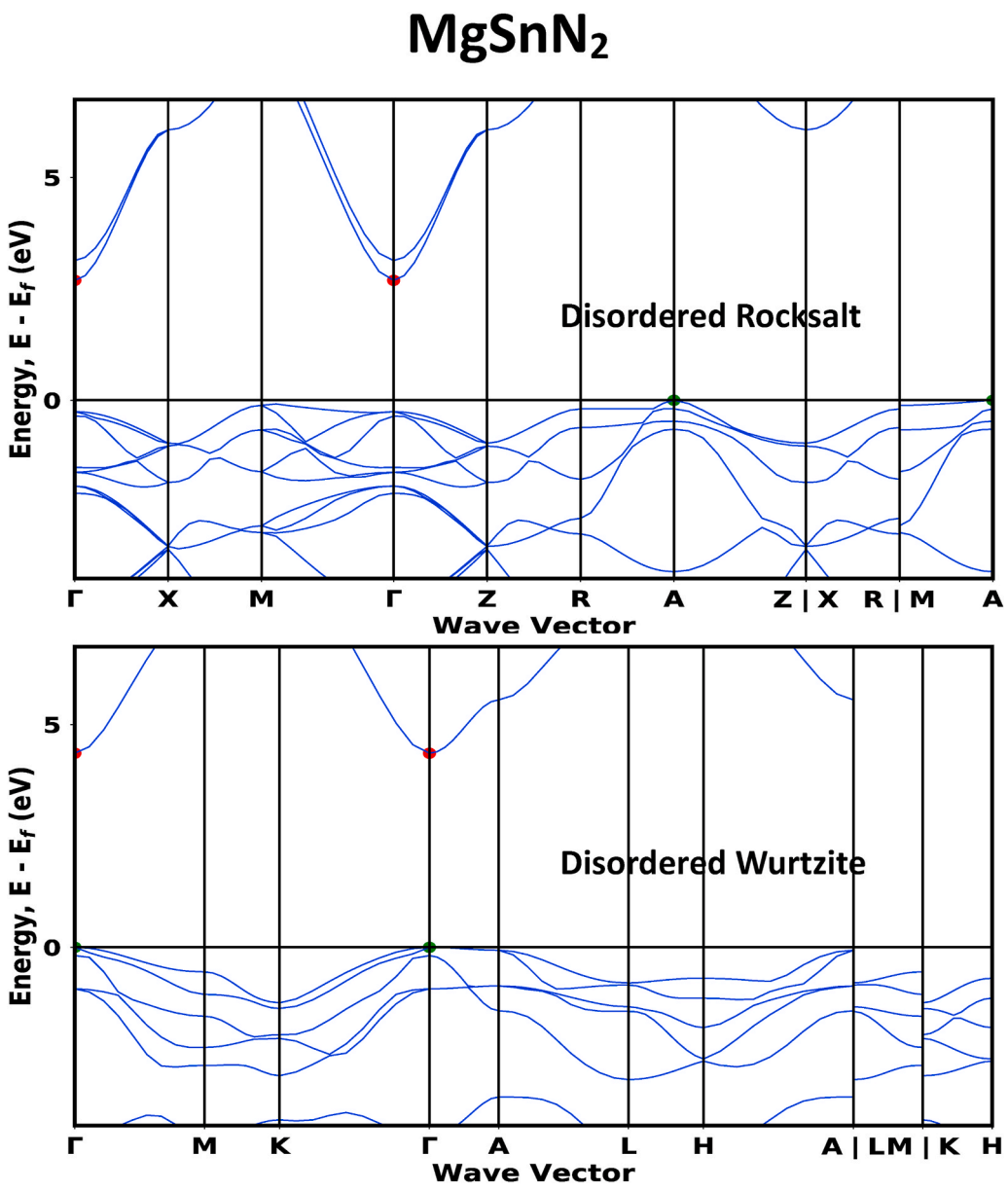

Fig. 2. Electronic band-structure diagrams of energy vs. wave vector for $MgSnN_2$ based on disordered rocksalt and wurtzite structures, computed using the HSE06 functional. Red dots represent conduction band minima; green dots represent valence band maxima. Fermi energy (E_f) is set at 0 eV.

compared to that from Mg to N is consistent with their reported electronegativities of 1.72 *e* for Sn and 1.23 *e* for Mg [94].

Fig. 2 shows the electronic band structure of $MgSnN_2$ computed using the hybrid HSE06 functional. The band structure of the orthorhombic form is not shown due to the high computing resources required. We computed the band gap of the disordered rocksalt structure as 2.69 eV, where the transition is from k-point A(0.5, 0.5, 0.5) to Γ(0, 0, 0), which is comparable to the experimental value of 2.3 eV determined by Kawamura et al. [24]. Greenaway et al. computed indirect band gaps of 3.17 and 2.93 eV for their two different disordered rocksalt structures, consistent with our findings. The experimentally reported band gap is a direct transition [24]. As discussed earlier in Section 3.1, experimental measurements revealed a possible oxygen impurity of 9.4% in the anionic positions [24]. Greenaway et al. [34] also found oxygen in their experimentally synthesized crystals of the disordered rocksalt and wurtzite phases. Thus, we calculated band gaps for disordered rocksalt $MgSnN_{1.5}O_{0.5}$, MgSnNO, and $MgSnN_{0.5}O_{1.5}$ using HSE06. All of these band gaps were evaluated as 0 eV, as shown in Table 2. As discussed above, Supplementary Fig. S4 shows the metallicity of these materials, since the valence band and conduction band have no gap. Unfortunately, the precise experimental concentration of O of 9.4%, as inferred from the EDX data, could not be simulated due to prohibitive computational requirements. We also calculated the band gap for disordered rocksalt $MgSnO_2$ using HSE06, obtaining a value of 1.01 eV, where the transition is direct at k-point A. This result suggests that nitrogen and oxygen together in the rocksalt structure as described here render the whole structure metallic. Our results suggest that there is some band-gap bowing in $MgSnN_{2-x}O_x$ (x = 0.0, 0.5. 1.0, 1.5, 2.0) that needs further exploration. Fig. S5 shows a band gap vs. oxygen content (x) diagram with bowing. The bowing suggests that the band gap will tend to a lower value. HSEO6-based computations are known to be successful in determining the band gaps of binary materials such as AlN and GaN close to their measured values [95–97]. For other materials, including ternary alloys such as $MgSnN_2$, this success has not been extensively verified. Nonetheless, our computed value of 2.69 eV is close to that reported for $Mg_{1.084}Sn_{0.916}N_{1.812}O_{0.188}$ [24]. Considering the difference in composition, that is, the presence of O in the experiment, the agreement is good. Table 2 lists the band-gap values in the other two crystal structures, orthorhombic and wurtzite, with the direct values at the Γ point being 4.86 and 4.36 eV, respectively.

During our computations, despite trying all permutations of the cation disordering in the disordered rocksalt and wurtzite phases, we did not observe any changes in the band gaps of the materials. This shows that the band gap is not tunable through cationic disorder in these two structures, at least for the limited cell sizes in our computations. However, Veal et al. and Makin et al. experimentally observed band-gap tunability in the disordered orthorhombic crystal structure [25,98]. We considered only one ordered orthorhombic structure in our calculations, due to limited computational resources, in which the cationic and anionic positions were fixed. Even if we had considered a disorder, we might have obtained similar characteristics for each disordered structure due to the limited cell size, as discussed above. Differences in the band gaps of the different phases may be connected to the bond lengths listed in Supplementary Table S8. Longer bonds lead to smaller band gaps, as observed in strained materials [99]. We note that the average of all bond lengths in the disordered rocksalt structure is higher than those in the other two phases, implying a smaller band gap. Although the averages of all bond lengths are equal in the orthorhombic and disordered wurtzite structures, the average bond lengths around Mg and Sn differ. As discussed above, Sn (1.72 *e*) is more electronegative than Mg (1.23 *e*) [94]. This expresses the greater tendency of Sn to control the behavior of electrons compared to Mg. We observe that the average bond length around Sn is shorter in the orthorhombic form than in the disordered wurtzite crystal, providing a rationale for the larger band gap in the former.

To provide insight into charge transport in these materials, we computed their effective masses. Table 2 lists the electron and hole effective masses in $MgSnN_{2-x}O_x$ for the different crystal structures calculated using the HSE06 functional. These are average values of different effective masses when charge carriers move between various k-points within the crystal at the valence band maximum (VBM) and conduction band minimum (CBM). In these calculations, we considered two bands in the VBM and one band in the CBM in the disordered rocksalt and wurtzite crystal structures, and one band in the CBM and one in the VBM in the orthorhombic crystal structure. It is clear that both electrons and holes in the disordered rocksalt structure have the lowest effective masses in comparison to the orthorhombic and disordered wurtzite crystal structures. Thus, this crystal structure is the best form of $MgSnN_2$ for charge transport. The hole effective mass is larger in this phase, as evidenced by the m_h/m_e ratio of 8.27. Moreover, the effective masses in the disordered rocksalt structure are comparable to those in silicon [100], making it favorable for solar applications. Though the effective masses are comparable to those in Si, the mobility in these disordered structures may be lower owing to the possibility of strong alloy scattering [101]. Electron effective masses are also smaller than those of holes in wurtzite and orthorhombic crystals, with the latter having the highest absolute values.

3.3. Optical properties

Orthorhombic and disordered wurtzite crystal structures are anisotropic in their interactions with photons, whereas disordered rocksalt is isotropic. The orthorhombic form is anisotropic in all three directions, whereas wurtzite is anisotropic in the parallel (∥) and perpendicular (⊥) directions with respect to the *xy* plane. The dielectric constant of Si is 11.7 [102], far higher than those of the disordered rocksalt (3.2), orthorhombic (2.1), and disordered wurtzite (2.6) crystal structures of $MgSnN_2$, considering the average of various directions in the latter two cases. These lower dielectric constants reduce the probability of charge separation due to the weakly screened coulombic attraction, thereby

Table 2
Band gaps and effective masses of $MgSnN_{2-x}O_x$ in different crystal structures calculated using HSE06. Units are in terms of standard electron rest mass, m_o. Experimental values are given in parentheses.

Material	Crystal Structure		Band Gap (eV)		Effective Mass (m*)	
	Name	Space Group	GGA	HSE06	Electron (m_e/m_o)	Hole (m_h/m_o)
$MgSnN_2$	disordered rocksalt	*P4/mmm*	0	2.69; indirect, (2.3; direct)[a]	0.26	2.15
$MgSnN_2$	disordered wurtzite	*P3m1*	2.47; direct	4.36; direct	0.69	4.75
$MgSnN_2$	orthorhombic	$Pna2_1$	2.84; direct	4.86; direct, 3.43; direct[b], 2.28; direct[c]	0.47	2.46
$MgSnN_{1.5}O_{0.5}$	disordered rocksalt	*P4/mmm*	0	0	–	–
MgSnNO	disordered rocksalt	*P4/mmm*	0	0	–	–
$MgSnN_{0.5}O_{1.5}$	disordered rocksalt	*P4/mmm*	0	0	–	–
$MgSnO_2$	disordered rocksalt	*P4/mmm*	0.01; indirect	1.01; direct	4.093	1.506

[a] Ref. [24].
[b] Ref. [33].
[c] Ref. [84].

reducing the efficiency of solar cells [103]. Of the three phases, disordered rocksalt is a better candidate as an absorber layer in solar cells because of its comparatively higher dielectric constant of 3.2. Complex dielectric function data for photon energies 0–10 eV are provided in Supplementary Tables S11 and S12.

The complex dielectric functions for the disordered rocksalt, orthorhombic, and disordered wurtzite crystal structures are presented in Figs. S6, S7, and S8, respectively. For all three phases, the real part shows a first peak around the band gap of each material in each direction. Similarly, the imaginary parts show some positive values after the band gap for each material. In the real part of the complex dielectric function, the disordered rocksalt crystal structure has a peak value of 4.1 at a photon energy of 3.26 eV, the disordered wurtzite crystal structure has peak values of 3.4 and 3.5 at photon energies of 4.68 and 4.66 eV in the $\perp$ and $\parallel$ directions, respectively, and the orthorhombic crystal structure has a peak value of 3.1 at a photon energy of 5.27 eV in all directions. After the first peak, the real part declines in all of the crystal structures, showing other prominent peaks later. The imaginary portion of the dielectric function also shows various peaks, attributable to several inter- and intra-band transitions [104].

Plots of absorption coefficient and reflectivity versus photon energy are shown in Fig. 3 for all three crystal structures of $MgSnN_2$, where averages of various directions were considered for the orthorhombic and disordered wurtzite crystal structures. The spectral irradiance of the Air Mass 1.5 Global spectrum [105] is also plotted, along with the absorption coefficient for ease of comparison. It can be seen that absorption of the disordered rocksalt structure commences at 2.7 eV and then shows a steep rise from 3.2 eV to 3.5 eV. For the orthorhombic and wurtzite crystal structures, absorption barely starts up to 3.5 eV. Hence, there is no reflection from these crystal structures between 1 eV and 3.5 eV, i.e., around the visible range. By comparing the spectral irradiance and absorption coefficient, it can be concluded that the disordered rocksalt structure may be used in the higher energy region of the visible range, whereas the orthorhombic and wurtzite structures will be of no use in visible range applications, but could be used as window layers in solar cells.

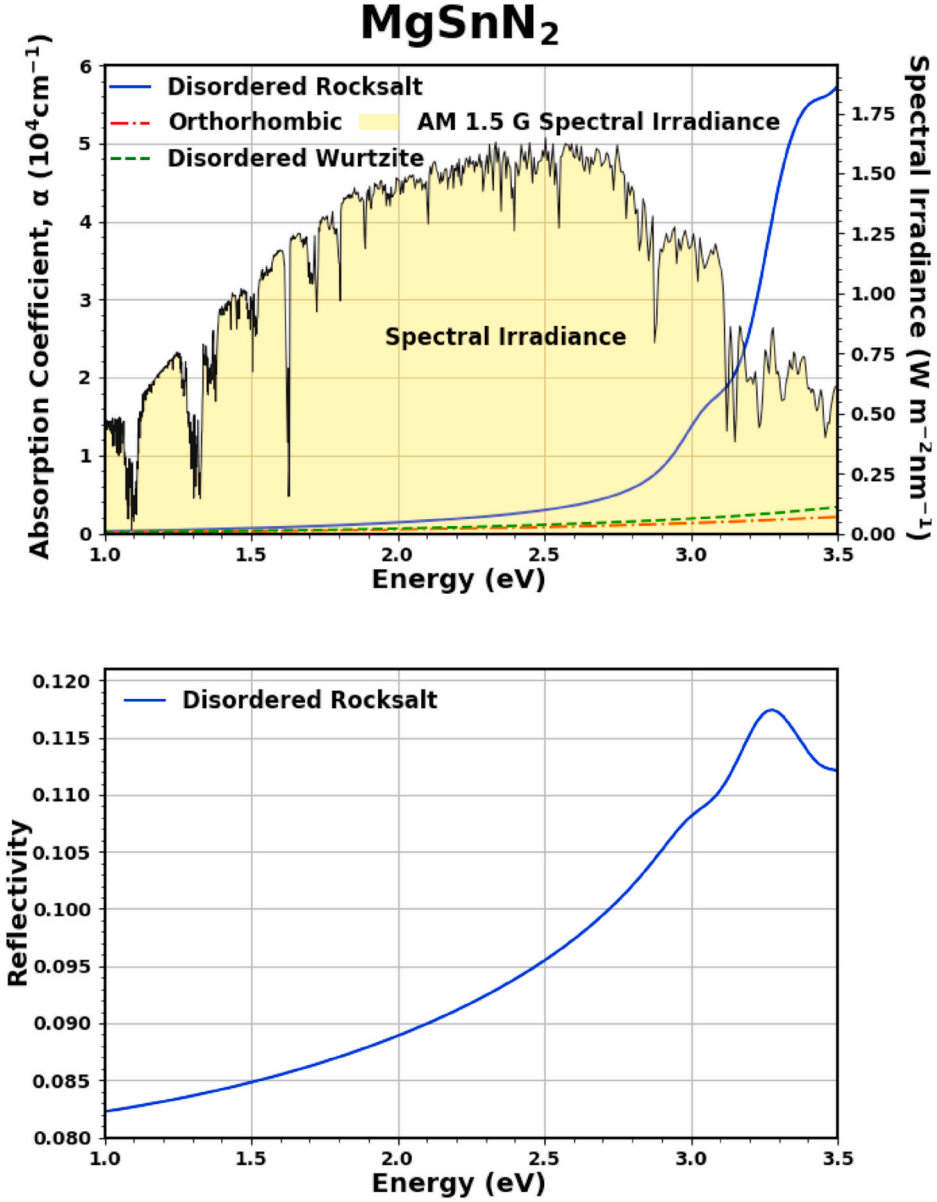

Fig. 3. Absorption coefficient, α (top panel), and reflectivity (bottom panel) curves, left axis, of $MgSnN_2$ based on rocksalt structure computed using the hybrid HSE06 functional. There is no reflection for orthorhombic and disordered wurtzite structures in the visible range. Standard AM 1.5 G solar spectral irradiance [105], right axis, is illustrated in the yellow shaded area along with the absorption curve.

4. Conclusion

We have computationally studied the structural, mechanical, vibrational, and opto-electronic properties of $MgSnN_2$ in three different crystal forms. Our study confirms that $MgSnN_2$ in the disordered rocksalt form is both mechanically and dynamically stable, as are the orthorhombic and disordered wurtzite crystal structures. Analysis of pCOHP curves, however, implies metastability. Our calculated lattice constant and electronic band-gap values of 4.56 Å and 2.69 eV for $MgSnN_2$ in the disordered rocksalt structure closely match the recent experimentally reported values of 4.48 Å and 2.3 eV, respectively. The computed band gap is indirect, while the experimentally reported one is direct [24]. We alloyed $MgSnN_2$ with oxygen to account for possible oxygen impurities. Computationally, the effect of alloying with oxygen implies a bowing of the band gap. Further experimental and theoretical work is necessary to explore the details of this bowing. Our study on effective masses has clarified that the disordered rocksalt structure has lower effective masses than the orthorhombic and disordered wurtzite crystal structures. Absorption coefficient and reflectivity curves validate that the disordered rocksalt structure might be used as an absorber layer in the higher energy region of the visible range in tandem devices, whereas the disordered wurtzite and orthorhombic crystal structures could serve as window layers of solar cells.

Declaration of competing interest

The authors declare that they have no known competing financial interests or personal relationships that could have appeared to influence the work reported in this paper.

Acknowledgements

All computing for this project was performed at the Ohio Supercomputer Center (OSC) [106]. We thank our funding sources: The National Science Foundation Division of Civil, Mechanical, and Manufacturing Innovation through grants 1629230 and 1629239, the University Cooperative Agreement High Specific Power Multi-Junction Thin Film Photovoltaics under Contract # FA9453-18-2-0037. The U. S. Government is authorized to reproduce and distribute reprints for Governmental purposes notwithstanding any copyright notation thereon. We also want to thank Dr. Richard Irving, of the Department of Physics and Astronomy, The University of Toledo, for his technical support in computing.

Appendix A. Supplementary data

Supplementary data to this article can be found online at https://doi.org/10.1016/j.jpcs.2021.110011.

Disclaimer

The views and conclusions contained herein are those of the authors and should not be interpreted as necessarily representing the official policies or endorsements, either expressed or implied, of Air Force Research Laboratory or the U.S. Government.

References

[1] S.R. Bauers, et al., Ternary nitride semiconductors in the rocksalt crystal structure, Proc. Natl. Acad. Sci. Unit. States Am. 116 (30) (2019) 14829–14834.
[2] D. Gall, et al., Electronic structure of ScN determined using optical spectroscopy, photoemission, and ab initio calculations, Phys. Rev. B 63 (12) (2001) 125119.
[3] E. Arca, et al., Redox-mediated stabilization in zinc molybdenum nitrides, J. Am. Chem. Soc. 140 (12) (2018) 4293–4301.
[4] F.A. Ponce, D.P. Bour, Nitride-based semiconductors for blue and green light-emitting devices, Nature 386 (6623) (1997) 351–359.
[5] U.K. Mishra, P. Parikh, Y.-F. Wu, AlGaN/GaN HEMTs-an overview of device operation and applications, Proc. IEEE 90 (6) (2002) 1022–1031.
[6] S. Nakamura, The roles of structural imperfections in InGaN-based blue light-emitting diodes and laser diodes, Science 281 (5379) (1998) 956–961.
[7] H. Amano, et al., Metalorganic vapor phase epitaxial growth of a high quality GaN film using an AlN buffer layer, Appl. Phys. Lett. 48 (5) (1986) 353–355.
[8] S. Nakamura, et al., Continuous-wave operation of InGaN/GaN/AlGaN-based laser diodes grown on GaN substrates, Appl. Phys. Lett. 72 (16) (1998) 2014.
[9] R.J. Trew, M.W. Shin, V. Gatto, High power applications for GaN-based devices, Solid State Electron. 41 (10) (1997) 1561–1567.
[10] K. Balasubramanian, S.V. Khare, D. Gall, Valence electron concentration as an indicator for mechanical properties in rocksalt structure nitrides, carbides and carbonitrides, Acta Mater. 152 (2018) 175–185.
[11] S. Kodambaka, et al., Absolute orientation-dependent anisotropic TiN(111) island step energies and stiffnesses from shape fluctuation analyses, Phys. Rev. B 67 (3) (2003), 035409.
[12] B.D. Ozsdolay, et al., *Cubic β-WN_x layers: Growth and properties vs N-to-W ratio*, Surf. Coating. Technol. 304 (2016) 98–107.
[13] X.-J. Chen, et al., Hard superconducting nitrides, Proc. Natl. Acad. Sci. Unit. States Am. 102 (9) (2005) 3198–3201.
[14] M. Wittmer, Properties and microelectronic applications of thin films of refractory metal nitrides, J. Vac. Sci. Technol. 3 (4) (1985) 1797–1803.
[15] A.D. Martinez, et al., *Synthesis, structure, and optoelectronic properties of II–IV–V_2 materials*, J. Mater. Chem. 5 (23) (2017) 11418–11435.
[16] D.H. Gregory, Structural families in nitride chemistry, J. Chem. Soc., Dalton Trans. (3) (1999) 259–270.
[17] J. Etourneau, J. Portier, F. Menil, The role of the inductive effect in solid state chemistry: how the chemist can use it to modify both the structural and the physical properties of the materials, J. Alloys Compd. 188 (1992) 1–7.
[18] B. Wang, et al., *Growth and properties of epitaxial Ti_{1-x} $Mg_xN(001)$ layers*, J. Vac. Sci. Technol.: Vacuum, Surfaces, and Films 36 (6) (2018), 061501.
[19] B. Wang, D. Gall, *Fully strained epitaxial $Ti_{1-x}Mg_xN(001)$ layers*, Thin Solid Films 688 (2019) 137165.
[20] B. Wang, D. Gall, *A New Semiconductor: $Ti_{0.5}Mg_{0.5}N$*, 001, in: *IEEE Nanotechnology Symposium (ANTS)*, 2018, Nanofab South Auditorium, SUNY Polytechnic Institute, Albany, NY 12203, 2018 (IEEE).
[21] V.S. Bhadram, et al., *Semiconducting cubic titanium nitride in the Th_3P_4 structure*, Physical Review Materials 2 (1) (2018), 011602.
[22] A.W. Jackson, et al., *Amorphous and nanocrystalline titanium nitride and carbonitride materials obtained by solution phase ammonolysis of $Ti(NMe_2)_4$*, J. Solid State Chem. 179 (5) (2006) 1383–1393.
[23] W.S. Williams, Transition-metal carbides, Prog. Solid State Chem. 6 (1971) 57–118.
[24] F. Kawamura, et al., *Synthesis of a novel rocksalt-type ternary nitride semiconductor $MgSnN_2$ using the metathesis reaction under high pressure*, Eur. J. Inorg. Chem. 2020 (5) (2020) 446–451.
[25] R.A. Makin, et al., Alloy-free band gap tuning across the visible spectrum, Phys. Rev. Lett. 122 (25) (2019) 256403.
[26] J.A. Ober, L.E. Apodaca, R.D. Crangle Jr., *Industrial minerals and sustainability: by-products from SO_2 mitigation as substitutes for mined mineral commodities*, GSA (Geol. Soc. Am.) Spec. Pap. (Reg. Stud.) 520 (2016) 79–87.
[27] M. Kneissl, et al., Advances in group III-nitride-based deep UV light-emitting diode technology, Semicond. Sci. Technol. 26 (1) (2011), 014036.
[28] T. Brokamp, H. Jacobs, Darstellung und Struktur einiger Gemischtvalenter ternärer tantalnitride mit lithium und magnesium, J. Alloys Compd. 183 (1992) 325–344.
[29] D.H. Gregory, et al., *Synthesis and structure of two new layered ternary nitrides, $SrZrN_2$ and $SrHfN_2$*, Inorg. Chem. 35 (26) (1996) 7608–7613.
[30] D.H. Gregory, et al., *Synthesis and structure of the new ternary nitride $SrTiN_2$*, Inorg. Chem. 37 (15) (1998) 3775–3778.
[31] D.H. Gregory, et al., *Synthesis, structure, and magnetic properties of the new ternary nitride $BaHfN_2$ and of the $BaHf_{1-x}Zr_xN_2$ solid solution*, J. Solid State Chem. 137 (1) (1998) 62–70.
[32] M. Råsander, M.A. Moram, *Elastic constants of the II–IV nitride semiconductors $MgSiN_2$, $MgGeN_2$ and $MgSnN_2$*, J. Phys. Appl. Phys. 51 (37) (2018) 375101.
[33] A.P. Jaroenjittichai, W.R.L. Lambrecht, *Electronic band structure of Mg−IV−N_2 compounds in the quasiparticle-self-consistent GW approximation*, Phys. Rev. B 94 (12) (2016) 125201.
[34] A.L. Greenaway, et al., Combinatorial synthesis of magnesium tin nitride semiconductors, J. Am. Chem. Soc. 142 (18) (2020) 8421–8430.
[35] G. Kresse, J. Furthmuller, Efficiency of ab-initio total energy calculations for metals and semiconductors using a plane-wave basis set, Comput. Mater. Sci. 6 (1) (1996) 15–50.
[36] G. Kresse, J. Furthmuller, Efficient iterative schemes for ab initio total-energy calculations using a plane-wave basis set, Phys. Rev. B 54 (16) (1996) 11169–11186.
[37] G. Kresse, J. Hafner, Ab initio molecular dynamics for liquid metals, Phys. Rev. B 47 (1) (1993) 558–561.
[38] G. Kresse, J. Hafner, Ab initio molecular-dynamics simulation of the liquid-metal–amorphous-semiconductor transition in germanium, Phys. Rev. B 49 (20) (1994) 14251–14269.
[39] J.P. Perdew, et al., Erratum: atoms, molecules, solids, and surfaces: applications of the generalized gradient approximation for exchange and correlation, Phys. Rev. B 48 (7) (1993) 4978.
[40] J.P. Perdew, et al., Atoms, molecules, solids, and surfaces: applications of the generalized gradient approximation for exchange and correlation, Phys. Rev. B 46 (11) (1992) 6671–6687.

[41] P.E. Blochl, Projector augmented-wave method, Phys. Rev. B 50 (24) (1994) 17953–17979.
[42] G. Kresse, D. Joubert, From ultrasoft pseudopotentials to the projector augmented-wave method, Phys. Rev. B 59 (3) (1999) 1758–1775.
[43] A. Jain, et al., Commentary: the Materials Project: a materials genome approach to accelerating materials innovation, Apl. Mater. 1 (1) (2013) 11.
[44] I.S. Khare, et al., Electronic, optical, and thermoelectric properties of sodium pnictogen chalcogenides: a first principles study, Comput. Mater. Sci. 183 (2020) 109818.
[45] V. Adhikari, et al., *First-principles study of mechanical and magnetic properties of transition metal (M) nitrides in the cubic M_4N structure*, J. Phys. Chem. Solid. 120 (2018) 197–206.
[46] N.J. Szymanski, et al., *Prediction of improved magnetization and stability in $Fe_{16}N_2$ through alloying*, J. Appl. Phys. 126 (9) (2019), 093903.
[47] X. Wu, D. Vanderbilt, D.R. Hamann, Systematic treatment of displacements, strains, and electric fields in density-functional perturbation theory, Phys. Rev. B 72 (3) (2005), 035105.
[48] V. Adhikari, et al., First principles investigation into the phase stability and enhanced hardness of TiN-ScN and TiN-YN alloys, Thin Solid Films 688 (2019) 137284.
[49] N.J. Szymanski, et al., Dynamical stabilization in delafossite nitrides for solar energy conversion, J. Mater. Chem. 6 (42) (2018) 20852–20860.
[50] K. Balasubramanian, S.V. Khare, D. Gall, Energetics of point defects in rocksalt structure transition metal nitrides: thermodynamic reasons for deviations from stoichiometry, Acta Mater. 159 (2018) 77–88.
[51] Z. Liu, et al., First-principles phase diagram calculations for the rocksalt-structure quasibinary systems TiN–ZrN, TiN–HfN and ZrN–HfN, J. Phys. Condens. Matter 29 (3) (2016), 035401.
[52] K. Balasubramanian, S. Khare, D. Gall, Vacancy-induced mechanical stabilization of cubic tungsten nitride, Phys. Rev. B 94 (17) (2016) 174111.
[53] K. Zhang, et al., Growth and mechanical properties of epitaxial NbN(001) films on MgO(001), Surf. Coating. Technol. 288 (2016) 105–114.
[54] K. Zhang, et al., *Epitaxial NbC_xN_{1-x}(001) layers: growth, mechanical properties, and electrical resistivity*, Surf. Coating. Technol. 277 (2015) 136–143.
[55] G. Grimvall, in: E. Wohlfarth (Ed.), *Thermophysical Properties of Materials, Ser.* Selected Topics in Solid State Physics, North-Holland, Amsterdam, 1986, p. 18.
[56] R. Hill, The elastic behaviour of a crystalline aggregate, Proc. Phys. Soc. 65 (5) (1952) 349–354.
[57] A. Reuss, Berechnung der fließgrenze von mischkristallen auf grund der plastizitätsbedingung für einkristalle, ZAMM–Journal of Applied Mathematics and Mechanics/Zeitschrift für Angewandte Mathematik und Mechanik 9 (1) (1929) 49–58.
[58] P.P. Gunaicha, et al., *Structural, energetic and elastic properties of $Cu_2ZnSn(S_xSe_{1-x})_4$ (x= 1, 0.75, 0.5, 0.25, 0) alloys from first-principles computations*, Sol. Energy 102 (2014) 276–281.
[59] X. Zhou, D. Gall, S.V. Khare, *Mechanical properties and electronic structure of anti-ReO_3 structured cubic nitrides, M_3N, of d block transition metals M: an ab initio study*, J. Alloys Compd. 595 (2014) 80–86.
[60] W. Voigt, Lehrbuch der kristallphysik, vol. 962, Teubner, Leipzig, 1928.
[61] Y. Tian, B. Xu, Z. Zhao, Microscopic theory of hardness and design of novel superhard crystals, Int. J. Refract. Metals Hard Mater. 33 (2012) 93–106.
[62] Z.T.Y. Liu, D. Gall, S.V. Khare, Electronic and bonding analysis of hardness in pyrite-type transition-metal pernitrides, Phys. Rev. B 90 (13) (2014) 134102.
[63] Z.T.Y. Liu, et al., First-principles investigation of the structural, mechanical and electronic properties of the NbO-structured 3d, 4d and 5d transition metal nitrides, Comput. Mater. Sci. 84 (2014) 365–373.
[64] Z.T.Y. Liu, et al., Structural, mechanical and electronic properties of 3d transition metal nitrides in cubic zincblende, rocksalt and cesium chloride structures: a first-principles investigation, J. Phys. Condens. Matter 26 (2) (2014), 025404.
[65] J. Paier, et al., Screened hybrid density functionals applied to solids, J. Chem. Phys. 124 (15) (2006) 154709.
[66] J. Heyd, G.E. Scuseria, M. Ernzerhof, Hybrid functionals based on a screened Coulomb potential, J. Chem. Phys. 118 (21) (2003) 8207–8215.
[67] A.V. Krukau, et al., Influence of the exchange screening parameter on the performance of screened hybrid functionals, J. Chem. Phys. 125 (22) (2006) 224106.
[68] N.J. Szymanski, et al., Electronic and optical properties of vanadium oxides from first principles, Comput. Mater. Sci. 146 (2018) 310–318.
[69] Z.T.Y. Liu, et al., *Transparency enhancement for $SrVO_3$ by $SrTiO_3$ mixing: a first-principles study*, Comput. Mater. Sci. 144 (2018) 139–146.
[70] B.B. Dumre, et al., *Improved optoelectronic properties in $CdSe_xTe_{1-x}$ through controlled composition and short-range order*, Sol. Energy 194 (2019) 742–750.
[71] A.M. Ganose, A.J. Jackson, D.O. Scanlon, Sumo: command-line tools for plotting and analysis of periodic ab initio calculations, The Journal of Open Source Software 3 (28) (2018) 717.
[72] V.L. Deringer, A.L. Tchougreeff, R. Dronskowski, Crystal orbital Hamilton population (COHP) analysis as projected from plane-wave basis sets, J. Phys. Chem. 115 (21) (2011) 5461–5466.
[73] R. Dronskowski, P.E. Blochl, Crystal orbital Hamilton populations (COHP). Energy-resolved visualization of chemical bonding in solids based on density-functional calculations, J. Phys. Chem. 97 (33) (1993) 8617–8624.
[74] S. Maintz, et al., Analytic projection from plane-wave and PAW wavefunctions and application to chemical-bonding analysis in solids, J. Comput. Chem. 34 (29) (2013) 2557–2567.
[75] S. Maintz, et al., LOBSTER: a tool to extract chemical bonding from plane-wave based DFT, J. Comput. Chem. 37 (11) (2016) 1030–1035.
[76] S. Maintz, M. Esser, R. Dronskowski, Efficient rotation of local basis functions using real spherical harmonics, Acta Phys. Pol. B 47 (4) (2016) 1165–1175.
[77] N.J. Szymanski, et al., Unconventional superconductivity in 3D rocksalt transition metal carbides, J. Mater. Chem. C 7 (40) (2019) 12619–12632.
[78] Z.T.Y. Liu, et al., First-principles phase diagram calculations for the rocksalt-structure quasibinary systems TiN–ZrN, TiN–HfN and ZrN–HfN, J. Phys. Condens. Matter 29 (3) (2017), 035401.
[79] G. Henkelman, A. Arnaldsson, H. Jónsson, A fast and robust algorithm for Bader decomposition of charge density, Comput. Mater. Sci. 36 (3) (2006) 354–360.
[80] E. Sanville, et al., Improved grid-based algorithm for Bader charge allocation, J. Comput. Chem. 28 (5) (2007) 899–908.
[81] W. Tang, E. Sanville, G. Henkelman, A grid-based Bader analysis algorithm without lattice bias, J. Phys. Condens. Matter 21 (8) (2009), 084204.
[82] M. Yu, D.R. Trinkle, Accurate and efficient algorithm for Bader charge integration, J. Chem. Phys. 134 (6) (2011), 064111.
[83] A. Togo, I. Tanaka, First principles phonon calculations in materials science, Scripta Mater. 108 (2015) 1–5.
[84] S. Lyu, W.R.L. Lambrecht, *Quasiparticle self-consistent GW band structures of Mg-IV-N_2 compounds: The role of semicore d states*, Solid State Commun. 299 (2019) 113664.
[85] K. Kanchiang, et al., *Structural and electronic properties of $MgGe_xSn_{(1-x)}N_2$ semiconductors: The density functional theory investigation*. Journal of Physics: Conference Series, IOP Publishing, 2018.
[86] S. Lany, et al., *Monte Carlo simulations of disorder in $ZnSnN_2$ and the effects on the electronic structure*, Physical Review Materials 1 (2017), 035401.
[87] D. Edström, et al., Effects of atomic ordering on the elastic properties of TiN- and VN-based ternary alloys, Thin Solid Films 571 (2014) 145–153.
[88] D.G. Sangiovanni, et al., Effects of phase stability, lattice ordering, and electron density on plastic deformation in cubic TiWN pseudobinary transition-metal nitride alloys, Acta Mater. 103 (2016) 823–835.
[89] N. Klasen, et al., FEM simulation of deformations in strings of shingled solar cells subjected to mechanical reliability testing. AIP Conference Proceedings, AIP Publishing LLC, 2019.
[90] F. Mouhat, F.-X. Coudert, Necessary and sufficient elastic stability conditions in various crystal systems, Phys. Rev. B 90 (22) (2014) 224104.
[91] J.P. Zanatta, et al., Growth of HgCdTe and CdTe(331)B on germanium substrate by molecular beam epitaxy, Appl. Phys. Lett. 71 (20) (1997) 2984–2986.
[92] S. Cole, M. Brown, A.F.W. Willoughby, *The microhardness of $Cd_xHg_{1-x}Te$*, J. Mater. Sci. 17 (7) (1982) 2061–2066.
[93] R.M. Hornreich, et al., Phonon band gaps, J. Phys. 7 (3) (1997) 509–519.
[94] A.L. Allred, E.G. Rochow, A scale of electronegativity based on electrostatic force, J. Inorg. Nucl. Chem. 5 (4) (1958) 264–268.
[95] Q. Guo, A. Yoshida, Temperature dependence of band gap change in InN and AlN, Jpn. J. Appl. Phys. 33 (5R) (1994) 2453–2456.
[96] A. Kyrtsos, M. Matsubara, E. Bellotti, *Band offsets of $Al_xGa_{1-x}N$ alloys using first-principles calculations*, J. Phys. Condens. Matter 32 (36) (2020) 365504.
[97] B. Monemar, Fundamental energy gap of GaN from photoluminescence excitation spectra, Phys. Rev. B 10 (2) (1974) 676.
[98] T.D. Veal, et al., *Band gap dependence on cation disorder in $ZnSnN_2$ solar absorber*, Advanced Energy Materials 5 (24) (2015) 1501462.
[99] N. Tit, I.M. Obaidat, H. Alawadhi, Origins of bandgap bowing in compound-semiconductor common-cation ternary alloys, J. Phys. Condens. Matter 21 (7) (2009), 075802.
[100] M.A. Green, Intrinsic concentration, effective densities of states, and effective mass in silicon, J. Appl. Phys. 67 (6) (1990) 2944–2954.
[101] B.E. Warren, B.L. Averbach, B.W. Roberts, Atomic size effect in the X-ray scattering by alloys, J. Appl. Phys. 22 (12) (1951) 1493–1496.
[102] C. Kittel, Introduction to Solid State Physics, John Wiley & Sons, New York, 2005.
[103] K.J.T. Hamam, Organic Solar Cells Based on High Dielectric Constant Materials: an Approach to Increase Efficiency, in: Western Michigan University: Graduate College at ScholarWorks at Western Michigan University, Department of Physics, 2013, p. 107.
[104] R. Deng, et al., Optical and transport measurement and first-principles determination of the ScN band gap, Phys. Rev. B 91 (4) (2015), 045104.
[105] N.R.E. Laboratory, Reference Air Mass 1.5 Spectra, 2003. https://www.nrel.gov/grid/solar-resource/spectra-am1.5.html.
[106] Ohio Supercomputer Center, 1987.